



Cobalt-substituted SrTi_{0.3}Fe_{0.7}O_{3-δ}: a stable high-performance oxygen electrode material for intermediate-temperature solid oxide electrochemical cells

Journal:	<i>Energy & Environmental Science</i>
Manuscript ID	EE-ART-02-2018-000449.R2
Article Type:	Paper
Date Submitted by the Author:	03-May-2018
Complete List of Authors:	<p>Zhang, Shanlin; Xi'an Jiaotong University, State Key laboratory for Mechanical Behavior of Materials, School of Materials Science and Engineering; Northwestern University, Department of Materials Science and Engineering</p> <p>Wang, Hongqian; Northwestern University, Department of Materials Science and Engineering</p> <p>Lu, Matthew; Northwestern University, Department of Materials Science and Engineering</p> <p>Zhang, Ai-Ping; Xi'an Jiaotong University, State Key laboratory for Mechanical Behavior of Materials, School of Materials Science and Engineering</p> <p>Mogni, Liliana; Centro Atomico Bariloche</p> <p>Liu, Qinyuan; Northwestern University, Department of Materials Science and Engineering</p> <p>Li, Chengxin; Xi'an Jiaotong University, School of material Science and engineering</p> <p>Li, Changjiu; Xi'an Jiaotong University, School of material Science and engineering</p> <p>Barnett, Scott; Northwestern University, Materials Science and Engineering</p>

Cobalt-substituted $\text{SrTi}_{0.3}\text{Fe}_{0.7}\text{O}_{3-\delta}$: a stable high-performance oxygen electrode material for intermediate-temperature solid oxide electrochemical cells†

Shan-Lin Zhang,^{a,b} Hongqian Wang,^a Matthew Y. Lu,^a Ai-Ping Zhang,^b Liliana V. Mogni,^c Qinyuan

Liu,^a Cheng-Xin Li,^b Chang-Jiu Li^{b,*} and Scott A. Barnett^{a,*}

^aDepartment of Materials Science and Engineering, Northwestern University, Evanston, Illinois 60208, USA

^bState Key laboratory for Mechanical Behavior of Materials, School of Materials Science and Engineering, Xi'an Jiaotong University, Xi'an, Shaanxi, 710049, People's Republic of China

^cCONICET-CNEA, Centro Atomico Bariloche, Av. Bustillo 9500, CP 8400, S.C.

Bariloche, Argentina

*Corresponding author. licj@xjtu.edu.cn, s-barnett@northwestern.edu

† Electronic supplementary information (ESI) available.

Abstract:

A key need in the development of solid oxide cells (SOCs) is for electrodes that promote fast oxygen reduction and oxygen evolution reactions at reduced operating temperature (≤ 700 °C), with sufficient durability to allow operation over desired 40,000 h lifetimes. A wide range of electrode materials have been investigated, with some providing resistance low enough for cell operation below 700 °C, but it is generally found that the electrode performance degrades over time. Here we demonstrate an oxygen electrode material, $\text{Sr}(\text{Ti}_{0.3}\text{Fe}_{0.7-x}\text{Co}_x)\text{O}_{3-\delta}$ (STFC), that provides a unique combination of excellent oxygen electrode performance and long-term stability. The addition of a relatively small amount of Co to $\text{Sr}(\text{Ti}_{0.3}\text{Fe}_{0.7})\text{O}_{3-\delta}$, e.g., $x = 0.07$, reduces the electrode polarization resistance by >2 times. The STFC electrode yields stable performance in both fuel cell and electrolysis modes at 1 A cm^{-2} . The fundamental oxygen diffusion and surface exchange coefficients of STFC are determined, and shown to be substantially better than those of $\text{La}_{0.6}\text{Sr}_{0.4}\text{Co}_{0.2}\text{Fe}_{0.8}\text{O}_{3-\delta}$, the most widely used SOC oxygen electrode material. While other electrode materials have been shown to exhibit better oxygen transport coefficients than STFC, they do not match its stability.

1. Introduction

Solid oxide cells (SOC) can be used both for converting fuels to electricity (solid oxide fuel cell mode)^{1, 2} and storing electricity as a chemical fuel (solid oxide electrolysis cell mode).^{3, 4} Solid oxide fuel cell systems provide an efficient and environment-friendly method for electrical generation using a wide variety of fuels including hydrogen and hydrocarbons. On the other hand, solid oxide electrolysis is being developed as a method for converting excess renewable electricity into fuels such as hydrogen, methane, gasoline, and methanol.^{5, 6} Alternatively, reversibly-operated solid oxide cells can be used as an electricity storage method.⁷ More widespread commercialization of these technologies will require reduced system cost and improved long-term durability. A reduction in cell operating temperature from current values, ~ 800 °C, to below 700 °C⁸⁻¹⁰ is expected to reduce cell degradation rates, e.g., by reducing Cr volatilization from interconnectors,^{11, 12} while also decreasing the costs of system balance-of-plant components.^{13, 14} Furthermore, system analyses indicate that the efficiency of CO₂-H₂O co-electrolysis can be increased via a reduction in cell operating temperature.^{3, 15}

The main processes limiting SOC power density are thermally activated, such that lowering the operating temperature increases cell area-specific resistance. A number of studies have shown that the oxygen electrode process, i.e., oxygen reduction reaction (ORR) in fuel cell mode and oxygen evolution reaction (OER) in electrolysis mode, provides the dominant resistance as operating temperature is reduced.^{4, 9, 16, 17} Thus, there has been a focus on developing high-activity oxygen electrode materials for reduced-temperature SOCs.^{18, 19} In order to reduce oxygen electrode polarization resistance at reduced operating temperature, there has been a shift from the widely-used La_{0.8}Sr_{0.2}MnO_{3- δ} -Zr_{0.84}Y_{0.16}O_{2- δ} (LSM-YSZ) composite electrode²⁰ to mixed ionically and electronically-conducting (MIEC) electrode materials.²¹⁻²³ In particular, La_{0.6}Sr_{0.4}Co_{0.2}Fe_{0.8}O_{3- δ} (LSCF)²⁴ is now used successfully in SOFC stacks by a number of developers, although electrode performance degradation has been observed due to Sr surface segregation hindering the oxygen surface exchange process.²⁵⁻²⁷ There have also been numerous reports of new oxygen electrode materials aimed at low-temperature operation.⁸ Much of this research has focused on perovskite materials with Co and/or Fe cations, e.g. La_xSr_{1-x}FeO_{3- δ} , La_xSr_{1-x}CoO_{3- δ} and Sm_xSr_{1-x}CoO_{3- δ} . A number of these materials contain Ba, including

(Ln,Ba)CoO_{3-δ} (Ln = La, Pr, etc.,) where ordering on the A-site may enhance performance, and Ba_{0.5}Sr_{0.5}Co_{0.8}Fe_{0.2}O_{3-δ} (BSCF),²⁸ which exhibits excellent performance even at temperature <600 °C. However, Ba surface segregation²⁹ and absorption of CO₂ make these materials unstable and there is typically rapid degradation during cell operation.³⁰ For example, the power density (at 750 °C and 0.8 V) of a cell with a BSCF cathode decreased from > 1 W cm⁻² to 0.45 W cm⁻² after 500 hours testing.³¹ Ln₂NiO_{4+δ} (Ln = La, Nd, Pr) MIEC oxides have shown promise as oxygen electrodes, exhibiting fast oxygen transport coefficients and good electrode performance.^{16, 32–34} However, these materials can be unstable under electrolysis operation,^{35, 36} for example, La₂NiO₄ was shown to decompose to high-order Ruddlesden-Popper La₃Ni₂O₇ and La₄Ni₃O₁₀ oxides at 750 °C during electrolysis.³⁵ Most electrodes are fabricated by powder processing, but liquid infiltration techniques have also been employed to produce highly-active nano-scale electrodes suitable for reduced-temperature SOCs.⁸ However, the ability to reduce polarization resistance by decreasing particle size is limited by particle coarsening that rapidly degrades performance.^{37, 38}

Relatively little has been reported on SrTiO₃-based oxygen electrodes. The application of Sr(Ti_{1-x}Fe_x)O_{3-δ} (STF) as an SOC electrode was suggested by early studies of its oxygen transport properties in membrane applications.³⁹ Tuller and co-workers subsequently carried out detailed studies of the properties of various STF compositions in thin-film form.^{40–45} Although electrical conductivities are not as high as some of the MIEC perovskites discussed above, competitive oxygen surface exchange and diffusion coefficients were observed for the more Fe-rich compositions. STF electrodes have the advantage of being composed of relatively inexpensive and earth-abundant elements, with no rare earths. In two studies of porous STF oxygen electrodes, the polarization resistance was acceptable for operation at 800 °C, but too high (≥ 0.5 Ω cm²) for operation at ≤ 700 °C.^{46, 47} STF has also been shown to be a good SOC fuel electrode material.^{48–50}

Here we report a comprehensive study of a new oxygen electrode composition, Sr(Ti_{0.3}Fe_{0.7-x}Co_x)O_{3-δ} (STFC) with $x = 0.04–0.15$. It is found that a relatively small amount of Co can improve the electrode performance significantly. Fundamental properties including thermal expansion, electronic conductivity, oxygen non-stoichiometry, and oxygen transport coefficients are reported, the latter using a combination of impedance spectroscopy, three-dimensional tomography, and oxide thermodynamic factor measurements. Results from > 1000 h life tests on symmetrical cells with La_{0.8}Sr_{0.2}Ga_{0.8}Mg_{0.2}O_{3-δ} (LSGM) electrolytes show the stable performance of the STFC electrodes. Single cells with

$\text{SrTi}_{0.3}\text{Fe}_{0.63}\text{Co}_{0.07}\text{O}_{3-\delta}$ oxygen electrode, conventional YSZ thin-film electrolyte and Ni-YSZ fuel electrode yielded good performance and stability at intermediate temperatures. Overall, the results show a unique combination of high stability and low polarization resistance at temperatures below 700 °C, suggesting that STFC is a highly desirable oxygen electrode material.

2. Results

2.1 Basic properties of STF and STFC: Phase composition, conductivity, oxygen nonstoichiometry, and thermal expansion coefficient

The XRD patterns from STF and STFC powders shown in Fig. 1 (a) have only peaks representative of the cubic perovskite structure. The STFC powders had no additional diffraction peaks assignable to free cobalt oxide, suggesting cobalt has substituted into the perovskite lattice. The cubic lattice parameters calculated from the XRD data decreased from 3.8859 ± 0.0005 Å to 3.81473 ± 0.0007 Å when the cobalt content increased from 0 to 15% (see Fig. S1, ESI†). This provides further evidence that Co is substituted into the perovskite structure. The decrease in lattice parameter agrees with the trend reported when an increasing amount of Co is substituted into $(\text{La,Sr})\text{FeO}_{3-\delta}$.⁵¹

Fig. 1 (b) shows the total electrical conductivities versus temperature for various compositions, which can be attributed to electronic conductivity since ionic conductivity is generally relatively low. The electrical conductivities gradually increased with increasing Co content, and all compositions showed a similar temperature dependence. Starting at low temperature, the conductivity increased first with increasing temperature, reached a maximum at ~400–500 °C, and then decreased. That is, the STF-based materials exhibited semiconductive behavior at low temperatures, but switched to metallic behavior at higher temperature, similar to prior reports for STF-based materials⁵² and other perovskites.⁵³ Increasing electronic conduction with increasing Co content is most probably associated with progressive delocalization of atomic levels and increasing bandwidth. Furthermore, the covalence of the $\text{Fe}^{3+}/\text{Fe}^{2+}$ –O bond is stronger than that of the $\text{Co}^{3+}/\text{Co}^{2+}$ –O bond, indicating decreased electron localization and increased electrical conductivity with increasing Co content.^{54–56} The maximum electrical conductivity values were observed at ~ 500 °C and ranged from 6.7 S cm^{-1} for STF ($x = 0$) to 24 S cm^{-1} for STFC-15 ($x = 0.15$). These values should be sufficient for applications in thin (~ 20 μm) electrode functional layers, but it may be desirable to use higher-conductivity materials, e.g., LSM or

LSCF, in the current collector layer.

The oxygen nonstoichiometry $3-\delta$ of STF and STFC-07 ($x = 0.07$), measured versus oxygen partial pressure pO_2 at various temperatures using thermogravimetry, is shown in Fig. 1 (c). $3-\delta$ varies approximately linearly with $\log(pO_2)$ from 1 to 10^{-4} atm, is lower for STFC-07 than for STF, and decreases with increasing temperature. For example, at 700 °C in air ($pO_2 = 0.21$ atm), δ increases from 0.249 for STF to 0.316 for STFC-07. The δ value for STF is similar to that reported for $SrFeO_{3-\delta}$, ~ 0.22 at 700 °C in air.⁵⁷ Although the δ value for STFC-07 is lower than that of BSCF (~ 0.45),⁵⁸ it is higher than the value for SSC (~ 0.15)⁵⁹ at 700 °C in air. On the other hand, these δ values are ~ 10 times larger than for many common perovskite oxygen electrode materials: e.g., $\delta = 0.03$ for $La_{0.6}Sr_{0.4}Co_{0.2}Fe_{0.8}O_{3-\delta}$ at the same condition.⁶⁰

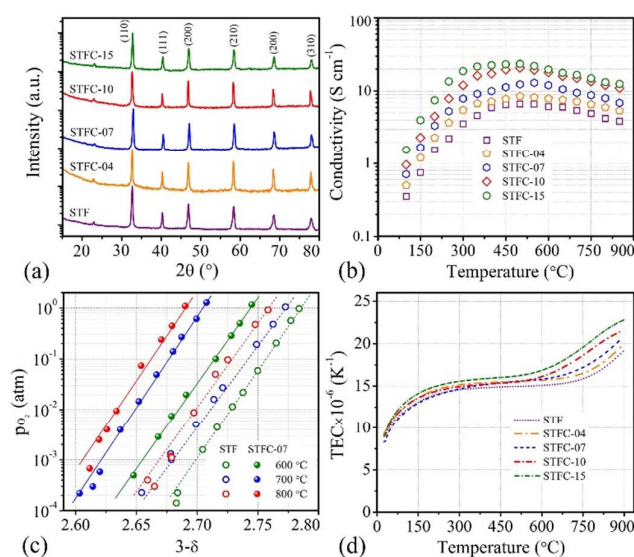


Fig. 1 Basic properties of STF and STFC: (a) XRD patterns, (b) total conductivity, (c) oxygen nonstoichiometry, and (d) thermal expansion coefficient.

Thermal expansion coefficients (TECs) in the temperature range 25–900 °C, calculated by fitting $\Delta L/L$ dilatometry data as a function of temperature, are shown in Fig. 1 (d). The TEC values were similar for all compositions below ~ 600 °C, starting at $9 \times 10^{-6} \text{ K}^{-1}$ at ambient temperature, first increasing and then reaching a plateau at $\sim 15 \times 10^{-6} \text{ K}^{-1}$ from ~ 200 – 600 °C, similar to reported data for other STF-based materials.^{47, 52} However, when the temperature is increased above 600 °C, the TEC increases rapidly, with larger increases for the higher Co compositions. The increase in TECs with increasing temperature and Co content is probably associated with the increased oxygen loss shown in Fig. 1 (c).⁵² Another factor that may lead to increasing thermal expansion at temperatures above 600 °C

is an increased disordering in the crystal lattice.⁵²

2.2 Microstructure and analysis of porous STF and STFC electrodes

A fracture cross-sectional scanning electron microscope (SEM) image of the STFC-07 electrode is shown in Fig. 2 (a). The electrode structure appears similar to that of many powder-processed porous electrodes reported previously.⁵⁰ As shown in Fig. S2 (ESI†), all of the STF and STFC electrode compositions showed morphologies essentially identical to that shown in Fig. 2 (a). Since the microstructure does not appear to vary with composition, the STFC-07 electrode was chosen as a representative case for detailed microstructural analysis. Fig. 2 (b) illustrates a typical 2D section from the 3D electrode microstructure measured by focused ion beam-SEM (FIB-SEM). Fig. 2 (c) shows the 3D image representation of a portion of the electrode. The images show that the electrode particles are well connected with each other and the electrolyte. Fig. 2 (d) shows the solid and pore size distributions and lists the microstructural data obtained from the 3D reconstruction. The electrode has a porosity of 41.45%. The mean STFC-07 solid particle size is ~ 375 nm, with a specific surface area $a = 8.04 \mu\text{m}^{-1}$, and a solid phase tortuosity factor of 1.14.

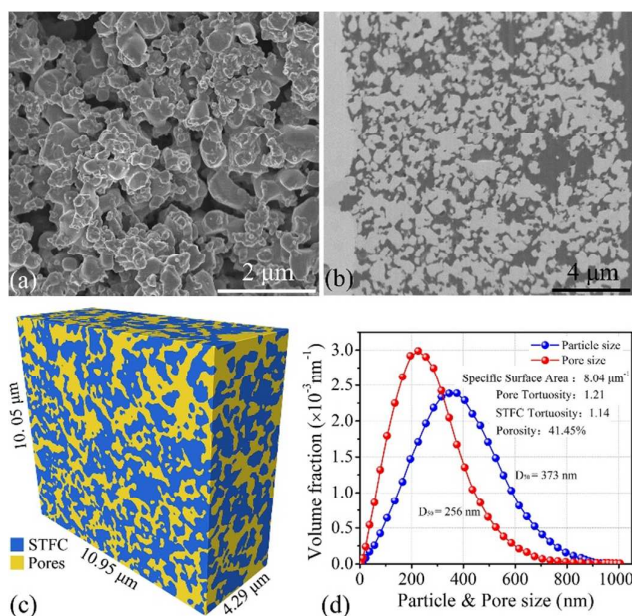


Fig. 2 Microstructure analysis of screen-printed STFC-07 electrodes; (a) fracture surface morphology; (b) Representative 2D section from the 3D data set; (c) 3D reconstruction obtained from FIB-SEM tomography; (d) calculated microstructural parameters.

2.3 Electrochemical Performance of symmetrical cells with STF and STFC oxygen electrodes

Fig. 3 shows Nyquist and Bode plots for the STF and STFC electrode symmetric cells, measured in air at (a) 600 and (b) 700 °C. The high-frequency real-axis intercepts of the impedance arcs are all within a narrow range ($\sim 0.45\text{--}0.5 \Omega \text{ cm}^2$ at 700 °C) and were as expected for these electrolyte thickness values. The data were thus plotted with the high frequency intercepts set to zero, in order to show clearly the changes in the polarization responses. Increasing the Co content caused a substantial decrease in the overall polarization resistance, with most of the decrease occurring between 0 and 7% Co. This was mainly due to a decrease in the dominant polarization response centered at ~ 2 to 200 Hz; the peak frequency generally shifted to lower frequency with increasing resistance, as expected. In the equivalent circuit used to fit the electrochemical impedance spectroscopy (EIS) data (Fig. S3 (ESI[†])), this response was fit with a modified Gerischer element (G). Examples of the fits obtained are shown in Fig. 3 and Fig. S3 (ESI[†]). Smaller responses at higher and lower frequencies were fit with R//QPE elements. The R2//QPE element at higher frequency, which is tentatively assigned to charge transfer between the electrode and electrolyte, was somewhat lower for STFC versus STF. The R3//QPE at low frequency (LF) did not vary significantly with cathode composition or temperature; this response can be associated with gas diffusion, which depends only on the electrode porosity and thickness, which did not appear to change with composition. The remainder of the equivalent circuit used to fit the EIS data (Fig. S3 (ESI[†])) consists of an inductor (L) primarily associated with measurement setup wires, the ohmic resistance (R1) associated with the electrolyte.

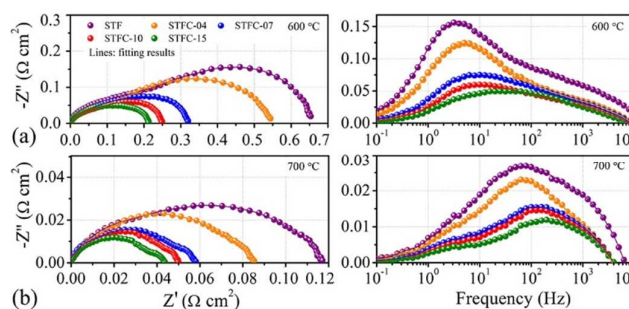


Fig. 3 Typical Nyquist (left) and Bode (right) plots of EIS data, measured at (a) 600 and (b) 700 °C. The high frequency intercepts in the data were set to zero, in order to facilitate comparison of the polarization arcs.

Fig. 4 gives a comparison of the total R_p versus inverse temperature for all the electrodes, obtained from the real-axis intercepts of EIS data such as that shown in Fig. 3 (a) and 3 (b). At 600 °C, $R_p = 0.65 \Omega \text{ cm}^2$ for STF, too high to allow effective low-temperature SOFC operation, but Co doping yields

more useful resistance values, *e.g.*, $0.32 \Omega \text{ cm}^2$ for STF-07 and $0.21 \Omega \text{ cm}^2$ for STF-15. At $700 \text{ }^\circ\text{C}$, Co doping also provides an important decrease in R_p , from $0.117 \Omega \text{ cm}^2$ for STF to $0.058 \Omega \text{ cm}^2$ for STF-07 and $0.043 \Omega \text{ cm}^2$ for STF-15. The STFC values are similar to values reported for similar conditions ($700 \text{ }^\circ\text{C}$ in air) for BSCF ($0.036 \Omega \text{ cm}^2$)⁶¹ and $\text{Sr}_{0.5}\text{Sm}_{0.5}\text{CoO}_{3-\delta}$ (SSC, $0.063 \Omega \text{ cm}^2$)⁶² but much lower than for LSCF ($\sim 0.16 \Omega \text{ cm}^2$)⁶³. The activation energy, calculated from linear fits to the $\ln(R_p)$ vs $1/T$ data in Fig. 4, increased from 1.15 eV for STF to 1.31 eV for STF-04, but then decreased with the further increase of Co doping to 1.13 eV for the STF-15 electrode. That is, the higher Co content STFC is more suitable for the application at lower temperatures.

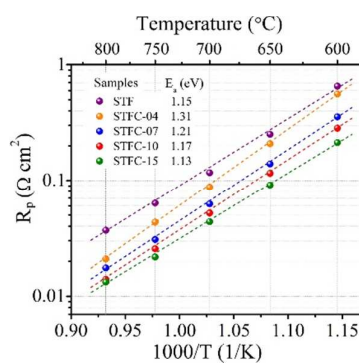


Fig. 4 Arrhenius plots of the electrode polarization resistance values measured from the real-axis intercepts on the Nyquist plots as shown in Fig. 3. These values were almost identical to those obtained from the equivalent circuit fits.

2.4 Stability of symmetrical cells with STF and STFC oxygen electrodes and Sr surface segregation

Stability is a key factor determining the practical utility of oxygen electrode materials. Thus, ~ 1000 h life tests were carried out at $700 \text{ }^\circ\text{C}$ on STF- and STFC-electrode symmetric cells, both with and without DC current. Fig. 5 shows the evolution of R_p with time for cells without (a) and with (b) current. There was typically an initial break-in period of ~ 50 h during which R_p decreased, *i.e.*, there was initial electrode activation, as reported for other oxygen electrode materials such as LSM-YSZ⁶⁴ and $\text{Pr}_2\text{NiO}_{4+\delta}$ -based electrodes³⁴. After the initial break-in, R_p remained stable, within measurement accuracy, for all the electrodes in the present study. Note that the cell ohmic resistance increased by $\sim 5\%$ during the life tests. As shown in Fig. S4 (ESI†), the increase was faster initially with the resistance tending to stabilize later in the test, and was similar with and without current. A similar resistance

increase was observed for cells with other electrodes. Thus, the ohmic resistance increase can be attributed to the slight conductivity degradation of the thick electrolyte,⁶⁵ and was not associated with the electrode.

Fracture cross sectional SEM images were taken from the STF and STFC-07 electrodes after ageing without current (Fig. S5 (ESI[†])) and with current on the SOFC side (Fig. S6 (ESI[†])) and on the SOEC side in (Fig. S7 (ESI[†])). The electrode surfaces appear identical to the unaged electrodes (Fig. S2 (ESI[†])). There are no signs of delamination or interfacial reactions in any case. The higher-magnification images show no signs of particle coarsening within the electrode after the ageing.

For comparison purposes, similar cells with LSCF electrodes were aged at the same condition for more than 800 h and the results are shown in Fig. 5 (c) and (d). These LSCF electrodes are essentially identical to those that have been characterized previously,⁶³ with microstructure similar to the present STFC electrodes (Fig. S16 (a) (ESI[†])). The ohmic resistance degraded $\sim 5\%$ after 800 h ageing (Fig. S8 (ESI[†])), which is consistent with the result from the symmetric cells with STFC electrodes as mentioned above (Fig. S4 (ESI[†])). The initial R_p for LSCF is $0.15\text{--}0.16\ \Omega\ \text{cm}^2$, which is higher than that of STF ($0.118\ \Omega\ \text{cm}^2$) and STFC ($0.056\ \Omega\ \text{cm}^2$) at $700\ ^\circ\text{C}$. In addition, R_p increased with time, reaching $> 0.2\ \Omega\ \text{cm}^2$ after 800 h ageing.

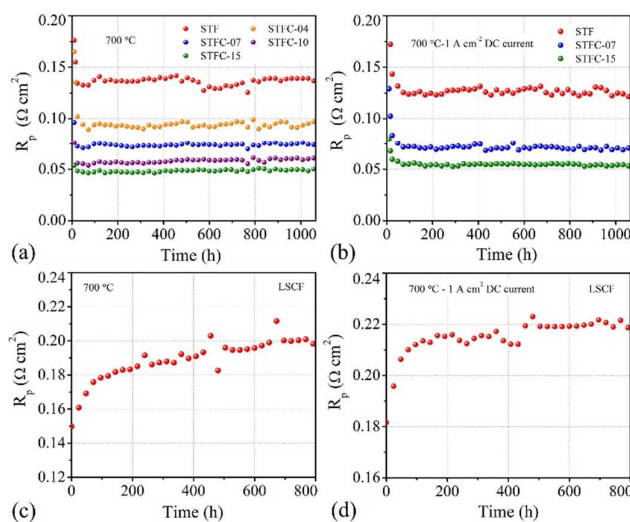


Fig. 5 Evolution of cell polarization resistance (R_p) at $700\ ^\circ\text{C}$ for the symmetric cells with STF-based and LSCF electrodes; (a) and (c) without current; (b) and (d) with $1\ \text{A cm}^{-2}$ DC current.

The surface composition of selected STF, STFC and LSCF electrodes were tested in the as-prepared state and after ageing in air at $700\ ^\circ\text{C}$ for 500 h. First, Sr surface segregation was assessed

using selective dissolution in ultrapure water and inductively coupled plasma optical emission spectrometry (ICP-OES) analysis,⁶³ with the results shown in Fig. 6 (a). The amount of Sr segregated on STF is much larger than that for LSCF. This may be attributed, at least in part, to the higher Sr content in STF (100% on the A site) compared to LSCF (40% on the A site). Second, the surface composition was analysed using X-ray Photoelectron Spectroscopy (XPS). Typical survey spectra from STF and STFC electrodes are shown in Fig. S9 (ESI†). The Sr peak intensity relative to the sum of the other cation peaks is plotted versus Co content in Fig. 6 (b). There is a clear decrease in the relative Sr intensity with increasing Co content, in agreement with Fig. 6 (a). The observation of Sr segregation on STF agrees with prior results on thin-film STF samples measured by XPS, where the surface Sr/(Ti+Fe) ratio ~ 1.7 for $\text{SrTi}_{0.3}\text{Fe}_{0.7}\text{O}_{3-\delta}$.⁶⁶ However, STFC with 7% and 15% Co showed much lower surface Sr than STF, closer to the values observed for LSCF. This may play a role in the reduced R_p observed for STFC compared to STF. It is unclear why the Co addition decreases Sr segregation. For the STF and STFC electrodes, the Sr segregation did not change after ageing, within experimental error. This is another key difference with LSCF, where the surface Sr content increases over time, as shown in Fig. 6(a) and also seen in numerous reports; this effect has been used to explain the performance degradation observed in LSCF.^{27, 63} Thus, the good stability of the STF and STFC electrodes may be explained, at least in part, by the stable amount of segregated Sr. On the other hand, it is not clear why the initial performance is very good despite the relatively large amount of segregated Sr present.

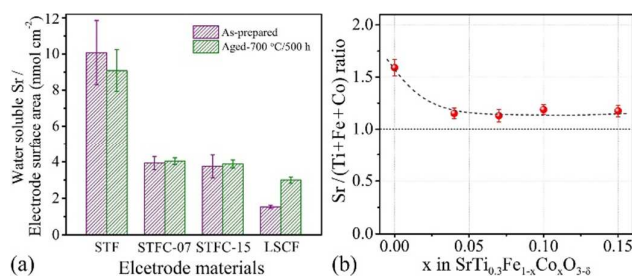


Fig. 6 (a) the amount of Sr on as-prepared and aged electrode surfaces, as measured by dissolution in ultrapure water. The detected amount was normalized by the electrode surface area and the error bars were calculated from standard deviation of 3 measurements; (b) Ratio of A- and B-site cations on electrodes surface as a function of Co content, measured by XPS.

2.5 Performance and stability of full cells with STFC-07 oxygen electrode

The STFC-07 oxygen electrodes were tested in full cells (Fig. S10, ESI†) to evaluate their performance under practical cell operating conditions. Fig. 7 (a) shows typical electrochemical characteristics under

representative fuel cell conditions, *i.e.*, in air and 3% H₂O+97% H₂ fuel. Peak power densities ranged from $> 2 \text{ W cm}^{-2}$ at 800 °C to $> 0.5 \text{ W cm}^{-2}$ at 600 °C, similar to other high-performance YSZ-electrolyte SOCs.^{67, 68} Fig. 7 (b) shows the voltage versus current density at different temperatures in electrolysis and fuel cell modes; the conditions are the same as in Fig. 7 (a), except that the fuel composition was 50% H₂O+50% H₂. At a typical electrolysis voltage of 1.3 V, the current densities are 3.03, 1.48, and 0.51 A cm⁻² at 800, 700, and 600 °C, respectively; these values are comparable to the best reported solid oxide electrolysis results.^{69, 70} The EIS data for the full cells, shown in Fig. S11 through S14 (ESI†), provides insights into the factors controlling the cell performance. For the cell measured in 50% H₂O + 50% H₂, the ohmic resistance is the main contribution at higher temperature, with the STFC oxygen electrode becoming more important at lower temperature. This may explain why the j-V curves show an approximately linear dependence at the higher temperatures, but show an activated behavior at lower temperatures. For the cell measured in 3% H₂O + 97% H₂, fuel electrode responses that were apparently related to gas diffusion and an electrochemical process had resistances comparable to those from the oxygen electrode. This may help explain why an apparent limiting current is seen in Fig. 7 (a) (3% H₂O + 97% H₂), but not in Fig. 7 (b) (50% H₂O + 50% H₂).

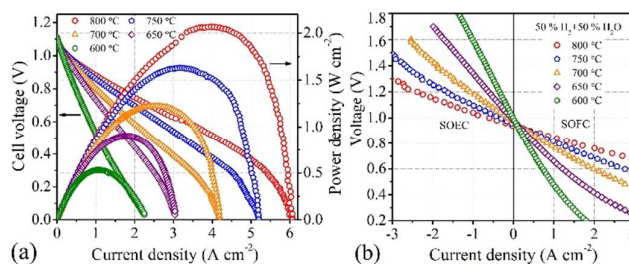


Fig. 7 Voltage and power density versus current density for a full cell with STFC-07 electrode measured at different temperatures in air and 3% H₂O humidified hydrogen. (b) Voltage versus current density measured at different temperatures in air and 50 vol.% H₂+50 vol. % H₂O.

Initial results on full solid oxide fuel cell stability are shown in Fig. 8. Cells with the STFC-07 and LSCF oxygen electrodes, but otherwise identical, were tested for 350 h at 700 °C, with the cell current maintained first at 1.0, then 1.2, and finally 1.5 A cm⁻² for the STFC-07 cell (the test was terminated after 250 h for the LSCF cell due to the low voltage). The initial voltage is higher for the STFC-07 electrode versus the LSCF electrode. During each constant current segment, the STFC-07 cell voltage decreased slightly, but the decrease was much less than that observed for the LSCF-electrode cell. EIS data from the STFC-07 cell before and after 250 h of testing showed that R_p did not change within

measurement accuracy, with most of the cell resistance increase coming from an increase in ohmic resistance (Fig. S15, ESI†). For comparison, the R_p increase in the LSCF cells was substantial, and appeared in the response at ~ 100 Hz, which could be associated with either the anode or the cathode. Comparison with the STFC-07 cell, where there was little degradation, and the results for LSCF-electrode symmetric cells, suggests that the R_p increase was associated with the LSCF. Fracture cross sectional SEM images showed no obvious changes in STFC-07 electrode microstructure after the life test (Fig. S16 (a) and (b), ESI†). For comparison, the microstructure of LSCF cathode had changed after 250 hours of testing (Fig. S16 (c) and (d) (ESI†)), with many nano-sized particles having formed on the LSCF surfaces. These may be segregated SrO particles.²⁷

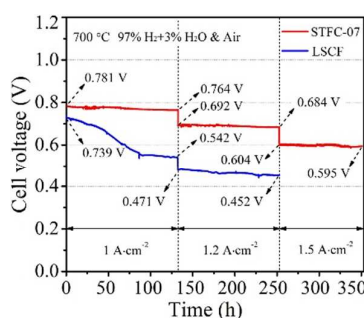


Fig. 8 Cell voltage versus time compared for full cells with STFC-07 and LSCF electrodes, during testing in fuel cell mode at different current density values at 700 °C.

3. Discussion

3.1 Electrode polarization and oxygen transport coefficients

In previous studies, it was shown that EIS data combined with 3D tomographic data can be used in the Adler-Lane-Steele (ALS) model to determine the oxygen solid state diffusion coefficient D^* and the oxygen surface exchange coefficient k^* .⁷¹⁻⁷³ This analysis is carried out here to obtain these fundamental transport parameters for STFC electrodes. These values are useful for understanding the reasons for the good electrode performance, and for making comparisons between STFC and other materials independent of electrode microstructure. The relevant expressions are given in the supplement. The Gerischer resistance R_G and time constant t_G values from the EIS fitted Gerischer response (Table S1, ESI†) are used along with the electrode porosity, surface area, and solid-phase tortuosity (given in Fig. 2). The other parameters needed include the oxygen vacancy concentration and thermodynamic factor, which were determined from the thermogravimetric data shown in Fig. 1 (c)

and are given in Table S2 (ESI†). The resulting D^* and k^* values are shown in Fig. 9. Both D^* and k^* are ~ 3 times higher for STFC-07 compared to STF. These increases may arise from the decreased Sr surface segregation for STFC-07 compared to STF; note that in one prior report on LSCF cathodes, both D^* and k^* were found to decrease with increasing Sr segregation.⁶³ Based on the ALS model expression for R_p (eq. S2, ESI†), the reduction in R_p caused by Co substitution can be explained by the increase in these oxygen transport coefficients, along with the small increase in oxygen vacancy concentration.

Fig. 9 also gives a comparison of D^* and k^* of STF and STFC-07 at 700 °C with other MIEC oxygen electrode materials that are known to exhibit fast oxygen transport. Compared to LSCF, both the D^* and k^* values at 700 °C for STFC-07 are ~ 10 times higher, while the D^* value is ~ 30 times higher at 600 °C. Since these increases are all expected to reduce R_p (see eq. S2, ESI†), this confirms that the substantially lower R_p reported here for STFC compared to LSCF is due to intrinsic materials property differences, not due to different electrode microstructures. Compared to BSCF, SSC, and LNO, the D^* value at 700 °C for STFC-07 is lower but within a factor of 5–10. k^* for STFC-07 at 700 °C is lower than SSC by a factor of ~ 2 , but is 5–8 times higher than BSCF and LNO. At a higher temperature (> 750 °C), STFC-07 shows the highest k^* value among these materials. Also, compared with the A-site ordered compound, GBCO, the D^* value for STFC-07 is ~ 8 –10 times higher, while the k^* value is ~ 10 –50 times higher. That is, the transport properties of STFC-07 are not too far from those of SSC and BSCF; as discussed further below, however, the stability of STFC-07 appears to be significantly better. Regarding the full cell test results, the relatively high current and power densities achieved are directly related to the relatively low polarization resistance of the STFC electrode. It should be possible to improve cell performance via various measures. At operating temperature ≥ 700 °C and low H_2O partial pressure, for example, gas diffusion through the anode support appears to contribute a major portion of the cell ASR, such that cell performance could potentially be improved by the use of a thinner or higher porosity support. At operating temperature < 700 °C, the oxygen electrode and YSZ electrolyte resistance are major contributors to the overall cell ASR. The results in Fig. 3 show that full cells with STFC-15 electrodes would provide lower oxygen electrode polarization than the STFC-07 used in the present cells, allowing higher power density. Furthermore, given the excellent stability of the STFC electrodes, it may be possible to microstructurally engineer these electrodes to provide even better low-temperature performance while maintaining the requisite

long-term stability. However, in order to achieve really good low-temperature cell performance, it will be necessary to reduce the electrolyte resistance, e.g. by utilizing an LSGM electrolyte instead of YSZ.^{78, 79}

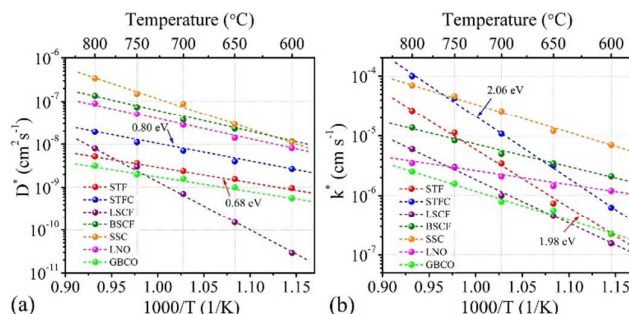


Fig. 9 (a) D^* and (b) K^* versus temperature for STF and STFC-07, and compared with other MIEC materials; STF: $\text{SrTi}_{0.3}\text{Fe}_{0.7}\text{O}_{3-\delta}$ (this study); STFC: $\text{SrTi}_{0.3}\text{Fe}_{0.63}\text{Co}_{0.07}\text{O}_{3-\delta}$ (this study); LSCF: $\text{La}_{0.6}\text{Sr}_{0.4}\text{Co}_{0.2}\text{Fe}_{0.8}\text{O}_{3-\delta}$ (Ref. 74); BSCF: $\text{Ba}_{0.5}\text{Sr}_{0.5}\text{Co}_{0.8}\text{Fe}_{0.2}\text{O}_{3-\delta}$ (Ref. 75); SSC: $\text{Sm}_{0.5}\text{Sr}_{0.5}\text{Co}_{3-\delta}$ (Ref. 74); LNO: $\text{La}_2\text{NiO}_{4+\delta}$ (Ref. 76); GBCO: $\text{GdBaCo}_2\text{O}_{5+\delta}$ (Ref. 77).

3.2 Electrode Stability

The symmetric cell life tests show excellent stability of the STFC electrodes, much better than the widely-used LSCF electrodes. It appears that the good stability can be explained, at least in part, by the stable amount of surface segregated Sr observed in life tests. Also, note that in the symmetric cell tests with current, one electrode operates as an SOFC cathode while the other operates as an SOEC anode. Thus, the STFC electrodes appear to provide excellent stability in both modes of operation. Good stability at 1 A cm^{-2} is especially notable given that most other oxygen electrodes degrade under electrolysis operation at this current density.^{80, 81} A key reason for this is probably the low R_p value, which leads to a relatively low electrode overpotential of $<0.12 \text{ V}$ during operation at $700 \text{ }^\circ\text{C}$ at 1 A cm^{-2} . This overpotential value, estimated using the measured electrode polarization resistance,⁸² is below the threshold value of $\sim 0.2 \text{ V}$ where degradation is normally observed, as expected based on an electrolyte fracture model.^{83, 84} The full cell life test, carried out in fuel cell mode, did show some degradation but it was mostly due to an increase in ohmic resistance. Noting that this test was relatively short, and that STFC electrode was stable in the symmetric cell, it may be that this degradation is just an early-stage cell break-in effect. More and longer life tests will be needed to clarify this. In summary, the STFC electrodes appear to be quite promising for solid oxide electrolysis and fuel cell operation, because of their stable performance at a relatively high current density.

Although some MIEC electrodes other than LSCF may provide better initial performance than the present STFC electrodes, degradation is often a serious problem. For example, BSCF³⁰ and SSC³⁷ electrodes provide excellent initial performance but degrade during the life tests due to surface segregation and absorption of CO₂ and SO₂.⁸⁵ For example, Giuliano et al.⁶¹ reported an initial R_p for BSCF at 700 °C of ~0.035 Ω cm², lower than that of STFC-15 (0.043 Ω cm²). However, after ageing at 700 °C for 200 h at a current density of 0.2 A cm⁻², R_p increased to 0.055 Ω cm² because of the Sr and Ba segregation. In contrast, the good stability presented in this study indicate that Sr surface segregation, while present, did not increase under cell operating conditions. Another means for reducing oxygen electrode polarization resistance is via MIEC materials with a nano-scale structure that provides high surface area, typically produced via impregnation.⁸⁶ While very good initial performance can be achieved, degradation via nanoparticle coarsening has been observed.³⁷ Recent results suggest that R_p values of ~ 0.2 Ω cm² can be achieved at 600 °C, similar to the present STFC-15 electrodes, for infiltrated LSCF^{87, 88} or SSC^{89, 90} electrodes. However, the present particle-based process is much easier to implement than the multiple impregnation steps required to make good nano-scale electrodes.

4. Summary and Conclusions

A comprehensive study of a new oxygen electrode composition, Sr(Ti_{0.3}Fe_{0.7-x}Co_x)O_{3-δ} (x = 0–0.15), is presented. Increasing substitution of Co into the oxide substantially increases electronic conductivity, reduces Sr surface segregation, reduces electrode polarization resistance, increases oxygen vacancy concentration, and increases both oxygen surface exchange rate and oxygen diffusion coefficient. A Co concentration x = 0.07 is suitable for cell operation ≥ 700 °C, but the lower polarization resistance achieved at x = 0.15 is desirable for cells operating as low as 600 °C. The electrodes are demonstrated to provide excellent performance in anode-supported solid oxide fuel cells.

The STFC electrodes compare very favorably with the LSCF electrodes widely used in state-of-the-art solid oxide fuel cells and electrolysis cells. Key advantages include the following:

(1) Polarization resistance values ~ 3x lower for electrodes with similar microstructure, with values low enough for operation down to ~ 600 °C for x=0.15;

(2) Improved oxygen transport kinetics, including > 100x higher oxygen surface exchange and oxygen diffusion coefficients, along with ~ 10x higher oxygen vacancy concentration;

(3) Superior performance stability, e.g. no measurable degradation observed during 1000 h life tests, compared to > 30% resistance degradation for LSCF electrodes under the same conditions;

(4) The electrode is composed of inexpensive earth-abundant materials, with no rare-earth elements and only a small amount of Co.

Although a number of MIEC electrodes have been developed that provide initially lower polarization resistance than STFC, these often exhibit significant stability issues or require challenging processing methods such as infiltration. Thus, it can be argued that these STFC electrodes provide a unique combination of low polarization resistance and stability useful for SOCs operating at temperatures as low as 600 °C.

5. Experimental

5.1 Materials synthesis and cell fabrication

Powders with compositions $\text{SrTi}_{0.3}\text{Fe}_{0.7}\text{O}_{3-\delta}$ (STF) and $\text{SrTi}_{0.3}\text{Fe}_{0.7-x}\text{Co}_x\text{O}_{3-\delta}$ with $x = 0.04$ (STFC-04), $x = 0.07$ (STFC-07), $x = 0.1$ (STFC-10), and $x = 0.15$ (STFC-15) were synthesized by solid state reaction. SrCO_3 (Sigma-Aldrich, 99.9%), TiO_2 (Alfa Aesar, 99.9%), Fe_2O_3 (Alfa Aesar, 99.8%), and $\text{Co}(\text{NO}_3)_2 \cdot 6\text{H}_2\text{O}$ (Alfa Aesar, 97.7%) were the starting materials. Stoichiometric amounts of the powders were ball milled in ethanol for 24 hours with zirconia balls as milling medium. The mixed powders were then dried and calcined at 1100 °C for 10 hours. The resulting STF and STFC powders were subsequently ball-milled in ethanol for another 48 hours as described above and dried.

The symmetrical cells had LSGM electrolytes with $\text{La}_{0.4}\text{Ce}_{0.6}\text{O}_{2-\delta}$ (LDC) barrier layers on both sides and identical STFC electrodes (Fig. S17 (ESI†)). We chose LSGM as the electrolyte in this case because of its high ionic conductivity, useful because of the much thicker electrolyte in the symmetrical cells. The sintered LSGM pellets (1450 °C/ 5 h) had a diameter of 14.5 mm and a thickness of ~ 0.5 mm. The 3–5 μm thick LDC interlayers, used to avoid possible chemical compatibility issues between the LSGM electrolyte and the electrode materials, were applied at both sides of the LSGM electrolyte by screen printing and subsequent firing at 1350 °C for 4 h. STF and STFC inks were prepared by mixing STF or STFC powders and binder (V-737, Heraeus) with weight

ratio of 1: 1.2 in a three-roll mill. The inks were then screen printed on both sides of the electrolyte pellet followed by firing at 1050 °C for 4 h. The electrode thickness was 10–15 µm and the electrode area was 0.5 cm². In order to compare the performance and stability of STF and STFC with LSCF, identical symmetric cells were prepared but with LSCF electrodes. Commercial LSCF powder (Praxair) was used to make the ink and the screen-printed electrodes were fired at 1100 °C for 2 h.

The full cells had a YSZ thin film electrolyte and thin GDC buffer layer. Ni/YSZ supported half cells were prepared by tape casting with 45 wt.% NiO + 45 wt. % YSZ + 10 wt.% starch (pore former) as the support layer, 50 wt.% NiO + 50 wt. % YSZ as the fuel electrode, and YSZ as the electrolyte. In order to reduce the firing temperature, 3% mol Fe₂O₃ was added in the electrolyte as the sintering aid.⁶⁷ Then the cells were co-fired at 1250 °C for 2 h. Next, in order to prevent any reactions between YSZ electrolyte and STF/STFC electrodes, a Gd_{0.1}Ce_{0.9}O_{2-δ} (GDC) interlayer was screen printed on the YSZ electrolyte and then fired at 1200 °C for 2 h. The STFC oxygen electrodes were screen printed onto the GDC interlayer and calcined at 1050 °C for 4 h. A cross sectional SEM image of a typical full cell, taken after testing, is shown in Fig. S8 (a) (ESI[†]). Similarly, full cells with LSCF electrodes were also prepared and the electrode was fired at 1100 °C for 2 h. The total effective area of the oxygen electrode is 0.5 cm².

5.2 Materials characterization

The phase structures of the STF and STFC powders were characterized via X-ray diffraction (XRD) analysis (Xpert PRO, PANalytical, Netherlands). Dense bar-shaped pellets with dimensions of ~5 mm × 5 mm × 25 mm, prepared by sintering at 1250 °C for 5 h, were used for conductivity and thermal expansion coefficient (TEC) measurements. The electrical conductivity was measured via a four-probe DC method with a Keithley 2400 source meter. The TEC was measured by a solid linear expansion coefficient apparatus (DIL 402C, NETZSCH). The oxygen nonstoichiometry for STF and STFC powders at different temperatures and different oxygen partial pressure (pO₂, 1~10⁻⁵ atm) were measured by a highly sensitive thermogravimetric setup.⁹¹ Cell microstructures were examined via scanning electron microscopy SEM (Hitachi SU8030) and FIB-SEM (FEI Helios) three-dimensional (3D) tomography analysis (described in detail elsewhere⁹²). The Sr surface segregation of as-prepared and aged STF, STFC, and LSCF electrodes was examined using selective chemical etching combined with inductively coupled plasma optical emission spectrometry (ICP-OES) detection, as described in detail elsewhere.^{27, 63} The surface composition of the electrodes was analyzed using X-ray

Photoelectron Spectroscopy (XPS, Thermo Fisher ESCALAB Xi⁺).

5.3 Electrochemical measurements for symmetric cells and full cells

For symmetric cells, gold contact grids were screen printed on both sides to facilitate current collection. The EIS measurements were conducted at 600–800 °C using an IM6 Electrochemical Workstation (ZAHNER, Germany) with a 20 mV AC signal in the frequency range of from 0.1 Hz to 100 kHz. The symmetric cells were life tested for > 1000 h at 700 °C with both electrodes exposed to ambient air, either without current or with a constant direct current of 1 A cm⁻² (Keithley 2420 power supply). The configuration of the test is shown in Fig. S17 (ESI[†]). In this condition, the electrode on one side was working under SOFC mode and other side was working under SOEC mode. EIS measurements were made once per day during the life tests, with no applied dc potential.

For the full cell testing, a silver grid (Heraeus Inc., Pennsylvania) was screen printed onto the oxygen electrode to enhance current collection. The cells were sealed onto alumina tubes with silver paste (DAD-87, Shanghai Research Institute of Synthetic Resins). For fuel cell testing, 100 sccm humidified H₂ (97% H₂+3% H₂O) was supplied to the Ni-YSZ anode while 150 sccm air was supplied to the STFC cathode, in the temperature range of 600–800 °C. For electrolysis testing, the oxygen electrode was exposed to air (150 sccm) while 100 sccm H₂ flowed through a heated H₂O-containing bubbler was supplied to the Ni-YSZ fuel electrode. In this study, the water in the bubbler was maintained at 81.7 °C, entraining 50 vol.% water in the H₂ flow. Current-voltage curves were measured at 10 mV increments over the relevant voltage ranges for fuel cell and electrolysis operation. Life tests were carried out at 700 °C with current densities from 1 A cm⁻² to 1.5 A cm⁻², for 350 hours.

Conflicts of interest

There are no conflicts to declare.

Acknowledgements

The authors at Northwestern University gratefully acknowledge financial support by the US Department of Energy Grant # DE-SC0016965, and US National Science Foundation grants DMR-1506925 (supported 3D tomography and associated analysis) and 1545907 (supported other microstructural characterization). Shan-Lin Zhang gratefully acknowledges the scholarship from the State Scholarship Fund of China Scholarship Council (201606285002). The authors at Xi'an Jiaotong

University acknowledge National Natural Science Foundation of China (Grant No. 51602248) for support of materials property measurements. The authors at Centro Atomico acknowledge AGNPCyT (PICT 2013-1032), CONICET and Universidad Nacional de Cuyo, which supported the thermogravimetric analysis. The authors also acknowledge the assistance of the Electron Probe Instrumentation Center (EPIC) at the NUANCE Center-Northwestern University, which has received support from the Soft and Hybrid Nanotechnology Experimental (SHyNE) Resource (NSF NNCI-1542205); the MRSEC program (NSF DMR-1121262) at the Materials Research Center; the International Institute for Nanotechnology (IIN); the Keck Foundation; and the State of Illinois, through the IIN. And the U.S. The authors also acknowledge Department of Energy's Office of Energy Efficiency and Renewable Energy (EERE) under the Fuel Cell Technologies Office (FCTO) under Award Number DE-EE 0008079.

References

1. B. C. H. Steele and A. Heinzl, *Nature*, 2001, **414**, 345.
2. E. D. Wachsman, C. A. Marlowe and K. T. Lee, *Energy Environ. Sci.*, 2012, **5**, 5498.
3. D. M. Bierschenk, J. R. Wilson and S. A. Barnett, *Energy Environ. Sci.*, 2011, **4**, 944-951.
4. C. Graves, S. D. Ebbesen, S. H. Jensen, S. B. Simonsen and M. B. Mogensen, *Nature Mater.*, 2014, **14**, 239.
5. Q. Fu, C. Mabilat, M. Zahid, A. Brisse and L. Gautier, *Energy Environ. Sci.*, 2010, **3**, 1382.
6. Y. Zheng, J. Wang, B. Yu, W. Zhang, J. Chen, J. Qiao and J. Zhang, *Chem. Soc. Rev.*, 2017, **46**, 1427.
7. L. Lei, Y. Wang, S. Fang, C. Ren, T. Liu and F. Chen, *Appl. Energy*, 2016, **173**, 52.
8. Z. Gao, L. V. Mogni, E. C. Miller, J. G. Railsback and S. A. Barnett, *Energy Environ. Sci.*, 2016, **9**, 1602.
9. C. Duan, D. Hook, Y. Chen, J. Tong and R. O'Hayre, *Energy & Environmental Science*, 2017, **10**, 176-182.
10. J. D. Baek, Y.-J. Yoon, W. Lee and P.-C. Su, *Energy Environ. Sci.*, 2015, **8**, 3374.
11. J. Li, D. Yan, W. zhang, J. Pu, B. Chi and L. Jian, *Electrochim. Acta*, 2017, **255**, 31.
12. H. Falk-Windisch, J. E. Svensson and J. Froitzheim, *J. Power Sources*, 2015, **287**, 25.
13. A. Dubois, S. Ricote and R. J. Braun, *J. Sources*, 2017, **369**, 65.

14. E. D. Wachsman and K. T. Lee, *Science*, 2011, **334**, 935.
15. S. H. Jensen, C. Graves, M. Mogensen, C. Wendel, R. Braun, G. Hughes, Z. Gao and S. A. Barnett, *Energy Environ. Sci.*, 2015, **8**, 2471.
16. A. Jun, J. Kim, J. Shin and G. Kim, *ChemElectroChem*, 2016, **3**, 511.
17. Y. Chen, W. Zhou, D. Ding, M. Liu, F. Ciucci, M. Tade and Z. Shao, *Adv. Energy Mater.*, 2015, **5**, 1500537.
18. L. Fan, B. Zhu, P. Su and C. He, *Nano Energy*, 2018, **45**, 148.
19. Y. Huang, A. M. Hussain and E. D. Wachsman, *Nano Energy*, 2018, **4**, 028.
20. Y. Itagaki, S. Watanabe, T. Yamaji, M. Asamoto, H. Yahiro and Y. Sadaoka, *J. Power Sources*, 2012, **214**, 153.
21. C. Zhang and K. Huang, *J. Power Sources*, 2017, **342**, 419.
22. L. Gao, Q. Li, L. Sun, X. Zhang, L. Huo, H. Zhao and J. Grenier, *J. Power Sources*, 2017, **371**, 86.
23. Y. Liu, S. Wang, Y. Hsu, H. Kai and P. Jasinski, *J. Eur. Ceram. Soc.*, 2018, **38**, 1654.
24. L. dos Santos-Gómez, J. M. Porras-Vázquez, E. R. Losilla, F. Martín, J. R. Ramos-Barrado and D. Marrero-López, *J. Power Sources*, 2017, **347**, 178.
25. Y. Liu, K. Chen, L. Zhao, B. Chi, J. Pu, S. P. Jiang and L. Jian, *Int. J. Hydrogen Energy*, 2014, **39**, 15868.
26. L. Zhao, J. Drennan, C. Kong, S. Amarasinghe and S. P. Jiang, *J. Mater. Chem. A*, 2014, **2**, 11114.
27. H. Wang and S. A. Barnett, *ECS Trans.*, 2017, **78**, 905.
28. Z. Shao and S. M. Haile, *Nature*, 2004, **431**, 170.
29. D. Garcés, H. Wang, S. A. Barnett, A. G. Leyva and L. V. Mognid, *ECS Trans.*, 2017, **78**, 1011.
30. Y. Liu, X. Zhu and W. Yang, *AIChE Journal*, 2015, **61**, 3879.
31. X. D. Zhou, J. W. Templeton, Z. Nie, H. Chen, J. W. Stevenson and L. R. Pederson, *Electrochim. Acta*, 2012, **71**, 44.
32. K. Zhao, Y.-P. Wang, M. Chen, Q. Xu, B.-H. Kim and D.-P. Huang, *Int. J. Hydrogen Energy*, 2014, **39**, 7120.
33. A. Murata, T. Uchikoshi and M. Matsuda, *J. Power Sources*, 2015, **293**, 95.
34. J. G. Railsback, Z. Gao and S. A. Barnett, *Solid State Ionics*, 2015, **274**, 134.
35. X. Tong, F. Zhou, S. Yang, S. Zhong, M. Wei and Y. Liu, *Ceram. Int.*, 2017, **43**, 10927.

36. S. J. Kim, K. J. Kim, A. M. Dayaghi and G. M. Choi, *Int. J. Hydrogen Energy*, 2016, **41**, 14498.
37. A. V. Call, J. G. Railsback, H. Wang and S. A. Barnett, *Phys. Chem. Chem. Phys.*, 2016, **18**, 13216.
38. M. Shah, P. W. Voorhees and S. A. Barnett, *Solid State Ionics*, 2011, **187**, 64.
39. V. V. Kharton, A. P. Viskup, A. V. Kovalevsky, F. M. Figueiredo, J. R. Jurado, A. A. Yaremchenko, E. N. Naumovich and J. R. Frade, *J. Mater. Chem.*, 2000, **10**, 1161.
40. W. Jung and H. L. Tuller, *Solid State Ionics*, 2009, **180**, 843.
41. A. Rothschild, W. Menesklou, H. L. Tuller and E. Ivers-Tiff, *Chem. Mater.*, 2006, **18**, 3651.
42. M. Kuhn, J. J. Kim, S. R. Bishop and H. L. Tuller, *Chem. Mater.*, 2013, **25**, 2970.
43. W. Jung and H. L. Tuller, *J. Electrochem. Soc.*, 2008, **155**, B1194.
44. W. Jung and H. L. Tuller, *Adv. Energy Mater.*, 2011, **1**, 1184.
45. Y. Chen, W. Jung, Z. Cai, J. J. Kim, H. L. Tuller and B. Yildiz, *Energy Environ. Sci.*, 2012, **5**, 7979.
46. S. Molin, W. Lewandowska-Iwaniak, B. Kusz, M. Gazda and P. Jasinski, *J. Electroceram.*, 2012, **28**, 80.
47. N. A. Baharuddin, A. Muchtar, M. R. Somalu, N. S. Kalib and N. F. Raduwan, *Int. J. Hydrogen Energy*, 2018, **01**, 210.
48. A. Nanning, L. Volgger, E. Miller, L. V. Mogni, S. Barnett and J. Fleig, *J. Electrochem. Soc.*, 2017, **164**, F364.
49. S. Cho, D. E. Fowler, E. C. Miller, J. S. Cronin, K. R. Poepfelmeier and S. A. Barnett, *Energy Environ. Sci.*, 2013, **6**, 1850.
50. T. Zhu, D. E. Fowler, K. R. Poepfelmeier, M. Han and S. A. Barnett, *J. Electrochem. Soc.*, 2016, **163**, F952.
51. L. W. Tai, M. M. Nasrallah, H. U. Anderson, D. M. Sparlin and S. R. Sehlin, *Solid State Ionics*, 1995, **76**, 259.
52. V. V. Kharton, A. V. Kovalevsky, A. P. Viskup, J. R. Jurado, F. M. Figueiredo, E. N. Naumovich and J. R. Frade, *J. Solid State Chem.*, 2001, **156**, 437.
53. S.-L. Zhang, K. Chen, A.-P. Zhang, C.-X. Li and C.-J. Li, *Ceram. Int.*, 2017, **43**, 11648.
54. L. Jiang, T. Wei, R. Zeng, W.-X. Zhang and Y.-H. Huang, *J. Power Sources*, 2013, **232**, 279.
55. J. Zou, J. Park, B. Kwak, H. Yoon and J. Chung, *Solid State Ionics*, 2012, **206**, 112.

56. J.-H. Kim and A. Manthiram, *J. Mater. Chem. A*, 2015, **3**, 24195.
57. Z. Zhang, Y. Zhu, Y. Zhong, W. Zhou and Z. Shao, *Adv. Energy Mater.*, 2017, **7**, 1700242.
58. J. Kim, S. Choi, A. Jun, H. Young Jeong, J. Shin and G. Kim, *ChemSusChem*, 2014, **7**, 1669.
59. S. Yoo, T.-H. Lim, J. Shin and G. Kim, *J. Power Sources*, 2013, **226**, 1.
60. H. J. M. Bouwmeester, M. W. Den Otter and B. A. Boukamp, *J. Solid State Electrochem.*, 2004, **8**, 599.
61. A. Giuliano, M. P. Carpanese, M. Panizza, G. Cerisola, D. Clematis and A. Barbucci, *Electrochim. Acta*, 2017, **240**, 258.
62. H. Lv, Y. Wu, B. Huang, B. Zhao and K. Hu, *Solid State Ionics*, 2006, **177**, 901.
63. H. Wang, K. J. Yakal-Kremiski, T. Yeh, G. M. Rupp, A. Limbeck, J. Fleig and S. A. Barnett, *J. Electrochem. Soc.*, 2016, **163**, F581.
64. G. Hughes, K. Yakal-Kremiski, A. Call and S. Barnett, *J. Electrochem. Soc.*, 2012, **159**, F858.
65. M. Morales, J. M. Perez-Falcon, A. Moure, J. Tartaj, F. Espiell and M. Segarra, *Int. J. Hydrogen Energy*, 2014, **39**, 5451.
66. W. Jung and H. L. Tuller, *Energy Environ. Sci.*, 2012, **5**, 5370.
67. Z. Gao, V. Y. Zenou, D. Kennouche, L. Marks and S. A. Barnett, *J. Mater. Chem. A*, 2015, **3**, 9955.
68. G. Yang, W. Zhou, M. Liu and Z. Shao, *ACS Appl. Mater. Inter.*, 2016, **8**, 35308.
69. R. Knibbe, M. L. Traulsen, A. Hauch, S. D. Ebbesen and M. Mogensen, *J. Electrochem. Soc.*, 2010, **157**, B1209.
70. M.-B. Choi, B. Singh, E. D. Wachsman and S.-J. Song, *J. Power Sources*, 2013, **239**, 361.
71. Y. Lu, C. Kreller and S. B. Adler, *J. Electrochem. Soc.*, 2009, **156**, B513.
72. K. Yakal-Kremiski, L. V. Mogni, A. Montenegro-Hernández, A. Caneiro and S. A. Barnett, *J. Electrochem. Soc.*, 2014, **161**, F1366.
73. J. Railsback, G. Hughes, L. Mogni, A. Montenegro-Hernández and S. A. Barnett, *J. Electrochem. Soc.*, 2016, **163**, F1433.
74. D. P. Rupasov, A. V. Berenov, J. A. Kilner, S. Y. Istomin and E. V. Antipov, *Solid State Ionics*, 2011, **197**, 18.
75. E. Bucher, A. Egger, P. Ried, W. Sitte and P. Holtappels, *Solid State Ionics*, 2008, **179**, 1032.

76. J.C. Grenier, F. Mauvy, C. Lalanne, J-M. Bassat, F. Chauveau, J. Mougín, J. Dailly and M. Marrony, *ECS Trans.*, 2009, **25**, 2537.
77. A. Taranco, S. J. Skinner, R. J. Chater, F. Hernández-Ramírez and J. A. Kilner, *J. Mater. Chem.*, 2007, **17**, 3175.
78. Z. Gao, E. C. Miller and S. A. Barnett, *Adv. Funct. Mater.*, 2014, **24**, 5703.
79. Z. Gao, H. Wang, E. Miller, Q. Liu, D. Senn and S. Barnett, *ACS Appl. Mater. Inter.*, 2017, **9**, 7115.
80. G. A. Hughes, K. Yakal-Kremiski and S. A. Barnett, *Phys. Chem. Chem. Phys.*, 2013, **15**, 17257.
81. M. S. Khan, X. Xu, J. Zhao, R. Knibbe and Z. Zhu, *J. Power Sources*, 2017, **359**, 104.
82. J. G. Railsback, Doctor of Philosophy, Phd Thesis, Northwestern University, 2016.
83. A. V. Virkar, *Int. J. Hydrogen Energy*, 2010, **35**, 9527.
84. A. V. Virkar, in *Engineered Ceramics*, John Wiley & Sons, Inc., 2016, **Ch4**, 59.
85. K. Yamaji, Y. Xiong, M. Yoshinaga, H. Kishimoto, M. Brito, T. Horita, H. Yokokawa, J. Akikusa and M. Kawano, *ECS Trans.*, 2009, **25**, 2853.
86. D. Ding, X. Li, S. Y. Lai, K. Gerdes and M. Liu, *Energy Environ. Sci.*, 2014, **7**, 552.
87. M. Liu, D. Ding, K. Blinn, X. Li, L. Nie and M. Liu, *Int. J. Hydrogen Energy*, 2012, **37**, 8613.
88. M. Shah and S. A. Barnett, *Solid State Ionics*, 2008, **179**, 2059.
89. F. Wang, D. Chen and Z. Shao, *J. Power Sources*, 2012, **216**, 208.
90. X. Lou, Z. Liu, S. Wang, Y. Xiu, C. P. Wong and M. Liu, *J. Power Sources*, 2010, **195**, 419.
91. A. Nenning, L. Volgger, E. Miller, L. Moggi, S. Barnett and J. Fleig, *J. Electrochem. Soc.*, 2017, **164**, F364.
92. K. Yakal-Kremiski, J. S. Cronin, Y. C. K. Chen-Wiegart, J. Wang and S. A. Barnett, *Fuel Cells*, 2013, **13**, 449.